results as the samples with small pH variations, thus indicating that the small variations in the effective net charge have no measurable influence on the cluster formation mechanism (see Supplementary Information). We also checked the temperature dependence of the pH for a concentrated lysozyme solution and found an increase of only 0.2 units when decreasing the temperature from 33 to 5 °C. Again, this results in a negligible charge variation when looking at the titration curve[25]. Lower concentrations were prepared by diluting the stock solution with buffer at pH 7.8. The samples with 50 mM NaCl were obtained by diluting a concentrated protein sample with HEPES buffer containing the appropriate amount of NaCl at pH 7.8. The final concentrations were determined by ultraviolet absorption spectroscopy at 280 nm using a specific absorption coefficient $E^{1\%}_{1\,cm} = 26.4$; the highest concentrations were typically between 250 and 350 mg ml^{-1}. Using a partial specific volume of 0.74 cm^3 g^{-1} for the proteins results in the corresponding protein monomer volume fractions of $0.185 \leq \phi \leq 0.26$.

Preparation of colloid–polymer mixtures

Spherical particles (radius $R = 660$ nm) with polymethylmethacrylate (PMMA) cores fluorescently labelled with nitrobenzoxadiazole and sterically stabilized by a thin (~10 nm) layer of chemically grafted poly-12-hydroxystearic acid were suspended in an approximately 1:4 mixture of *cis*-decalin and cycloheptyl bromide (CHB) for density matching. CHB leads to a positive charge Q of the PMMA particles[21] with $Q \leq 10^3$ electronic charges for the present particles (estimated from ϕ at crystallization). Addition of linear, non-adsorbing polystyrene (Polymer Laboratory, molecular mass 212.4 kDa) induces an effective attraction between the PMMA particles: exclusion of polymer between the surfaces of two nearby particles results in a net osmotic force that pushes them together[22]. The depth and range of this 'depletion' attraction are proportional to the polymer concentration and polymer size, respectively. Polymer size can be estimated by twice the radius of gyration r_g of a single coil, giving a dimensionless range $\delta \approx r_g/R$, here $\delta \approx 0.02$.

Small-angle X-ray scattering measurements

SAXS experiments were carried out with a pinhole camera (NanoSTAR, Bruker AXS) equipped with a sealed tube (Cu K_α), a thermostatically regulated sample chamber and a two-dimensional gas detector. The q range is 0.1–2 nm^{-1}.

Small-angle neutron scattering measurements

SANS experiments were performed at the SANS I facility at the Swiss neutron source SINQ at the Paul Scherrer Institut, Switzerland. We used 1-mm and 2-mm Hellma quartz cells and a thermostatically regulated sample holder. Combinations of different wavelengths (5 and 8 Å), sample-to-detector distances (1.6–18 m) and collimation lengths (4.5–18 m) were used to cover a q range of 0.1–7 nm^{-1}.

Confocal microscopy

Imaging was carried out in the Collaborative Optical Spectroscopy, Micromanipulation and Imaging Centre (COSMIC). A small amount of sample was sandwiched between a cover slip and a microscope slide. The sample thickness was fixed at about 0.3 mm by spacers. A Nikon TE-300 with a Biorad Radiance 2100MP scanning head was used; fluorescence was excited at 488 nm and observed at 525 nm.

Received 1 September; accepted 6 October 2004; doi:10.1038/nature03109.

1. Dawson, K. A. The glass paradigm for colloidal glasses, gels, and other arrested states driven by attractive interactions. *Curr. Opin. Colloid Interf. Sci.* **7,** 218–227 (2002).
2. Trappe, V., Prasad, V., Cipelletti, L., Segre, P. N. & Weitz, D. A. Jamming phase diagram for attractive particles. *Nature* **411,** 772–775 (2001).
3. Sciortino, F. Disordered materials: one liquid, two glasses. *Nature Mater.* **1,** 145–146 (2002).
4. Pham, K. N. *et al.* Multiple glassy states in a simple model system. *Science* **296,** 104–106 (2002).
5. Eckert, T. & Bartsch, E. Re-entrant glass transition in a colloid-polymer mixture with depletion attractions. *Phys. Rev. Lett.* **89,** 125701–125704 (2002).
6. Weeks, E. R., Crocker, J. C., Levitt, A. C., Schofield, A. & Weitz, D. A. Three-dimensional direct imaging of structural relaxation near the colloidal glass transition. *Science* **287,** 627–631 (2000).
7. Foffi, G. *et al.* Phase equilibria and glass transition in colloidal systems with short-ranged attractive interactions: application to protein crystallization. *Phys Rev. E* **65,** 031407–031417 (2002).
8. Bergenholtz, J., Poon, W. C. K. & Fuchs, M. Gelation in model colloid-polymer mixtures. *Langmuir* **19,** 4493–4503 (2003).
9. Kulkarni, A. M., Dixit, N. M. & Zukoski, C. F. Ergodic and non-ergodic phase transitions in globular protein suspensions. *Faraday Discuss.* **123,** 37–50 (2003).
10. Puertas, A. M., Fuchs, M. & Cates, M. E. Dynamical heterogeneities close to a colloidal gel. *J. Chem. Phys.* **121,** 2813–2822 (2004).
11. Sciortino, F., Mossa, S., Zaccarelli, E. & Tartaglia, P. Equilibrium cluster phases and low-density arrested disordered states: The role of short-range attraction and long-range repulsion. *Phys. Rev. Lett.* **93,** 055701 (2004).
12. Groenewold, J. & Kegel, W. K. Anomalously large equilibrium clusters of colloids. *J. Phys. Chem. B* **105,** 11702–11709 (2001).
13. Segré, P. N., Prasad, V., Schofield, A. B. & Weitz, D. A. Glasslike kinetic arrest at colloidal-gelation transition. *Phys. Rev. Lett.* **86,** 6042–6045 (2001).
14. Guillot, S., Delsanti, M., Désert, S. & Langevin, D. Surfactant-induced collapse of polymer chains and monodisperse growth of aggregates near the precipitation boundary in carboxymethylcellulose-DTAB aqueous solutions. *Langmuir* **19,** 230–237 (2003).
15. Muschol, M. & Rosenberger, F. Liquid-liquid phase separation in supersaturated lysozyme solutions and associated precipitate formation/crystallization. *J. Chem. Phys.* **107,** 1953–1962 (1997).
16. Pedersen, J. S., Hansen, S. & Bauer, R. The aggregation behavior of zinc-free insulin studied by small-angle neutron scattering. *Eur. Biophys. J.* **22,** 379–389 (1994).
17. Piazza, R. Interactions and phase transitions in protein solutions. *Curr. Opin. Colloid Interf. Sci.* **5,** 38–43 (2000).
18. Malfois, M., Bonnete, F., Belloni, L. & Tardieu, A. A model of attractive interactions to account for fluid-fluid phase separation of protein solutions. *J. Chem. Phys.* **105,** 3290–3300 (1996).
19. Broide, M. L., Tomic, T. M. & Saxowsky, M. D. Using phase transitions to investigate the effect of salts on protein interactions. *Phys. Rev. E* **53,** 6325–6335 (1996).
20. Schurtenberger, P., Chamberlin, R. A., Thurston, G. M., Thomson, J. A. & Benedek, G. B. Observation of critical phenomena in a protein-water solution. *Phys. Rev. Lett.* **63,** 2064–2067 (1989).
21. Yethiraj, A. & Van Blaaderen, A. A colloidal model system with an interaction tunable from hard sphere to soft and dipolar. *Nature* **421,** 513–517 (2003).
22. Poon, W. C. K. The physics of a model colloid-polymer mixture. *J. Phys. Condens. Matter* **14,** R859–R880 (2002).
23. Pham, K. N., Egelhaaf, S. U., Pusey, P. N. & Poon, W. C. K. Glasses in hard spheres with short-range attraction. *Phys. Rev. E* **69,** 11503–11516 (2004).
24. Rojas, L., Urban, C., Schurtenberger, P., Gisler, T. & Grünberg, H. H. Reappearance of structure in charge-stabilized suspensions. *Europhys. Lett.* **60,** 802–808 (2002).
25. Tanford, C. & Roxby, R. Interpretation of protein titration curves. Application to lysozyme. *Biochemistry* **11,** 2192–2198 (1972).

Supplementary Information accompanies the paper on **www.nature.com/nature**.

Acknowledgements We thank the Swiss spallation source at the Paul Scherrer Institut (PSI) in Villigen, Switzerland, for the neutron beam time and we acknowledge the help of our local contacts J. Kohlbrecher and S. van Petegem. We thank J. Groenewold, W. Kegel, F. Sciortino, K. Kroy and M. Cates for discussions. We thank A. Schofield for preparing the fluorescent PMMA particles. This work was supported by the Swiss National Science Foundation, the UK Engineering and Physical Sciences Research Council, the Scottish Higher Education Funding Council, and the Marie Curie Network on Dynamical Arrest of Soft Matter and Colloids. A.S. and P.S. conceived and performed the protein experiments; F.C. prepared the pH stabilized protein samples for the control experiments; H.S., W.C.K.P. and S.U.E. carried out and analysed the experiments with the colloid–polymer samples.

Competing interests statement The authors declare that they have no competing financial interests.

Correspondence and requests for materials should be addressed to P.S. (peter.schurtenberger@unifr.ch).

A humid climate state during the Palaeocene/Eocene thermal maximum

Gabriel J. Bowen[1]*, David J. Beerling[2], Paul L. Koch[1], James C. Zachos[1] & Thomas Quattlebaum[1]

[1]*Earth Sciences Department, University of California, Santa Cruz, California 95064, USA*
[2]*Department of Animal and Plant Sciences, University of Sheffield, Sheffield S10 2TN, UK*

* Present address: Department of Biology, University of Utah, Salt Lake City, Utah 84112, USA

An abrupt climate warming of 5 to 10 °C during the Palaeocene/Eocene boundary thermal maximum (PETM) 55 Myr ago is linked to the catastrophic release of ~1,050–2,100 Gt of carbon from sea-floor methane hydrate reservoirs[1]. Although atmospheric methane, and the carbon dioxide derived from its oxidation, probably contributed to PETM warming, neither the magnitude nor the timing of the climate change is consistent with direct greenhouse forcing by the carbon derived from methane hydrate. Here we demonstrate significant differences between marine[2,3] and terrestrial[4–6] carbon isotope records spanning the PETM. We use models of key carbon cycle processes[7–9] to identify the cause of these differences. Our results provide evidence for a previously unrecognized discrete shift in the state of the climate system during the PETM, characterized by large increases in mid-latitude tropospheric humidity and enhanced cycling of carbon through terrestrial ecosystems. A more humid atmosphere helps to explain PETM temperatures, but the ultimate mechanisms underlying the shift remain unknown.

Global warming during the PETM is associated with a major negative carbon isotope ($\delta^{13}C$, see Fig. 1 legend) excursion (CIE), which has been invoked as evidence for the release of ^{13}C-poor carbon from methane hydrate reservoirs into the ocean and atmosphere[1]. The signature of this carbon release is a rapid and synchronous decrease in the $\delta^{13}C$ of carbon in terrestrial[4–6,10] and marine[2,3] rocks (Fig. 1). The $\delta^{13}C$ values stabilize approximately 35 kyr after the beginning of the event, indicating the cessation of methane release. Throughout the following ~45 kyr, $\delta^{13}C$ values remain relatively low and then begin an exponential recovery lasting for some ~50 kyr. Temperature, in contrast, rises steadily from the beginning of the event to a peak ~60 kyr later, and gradually declines to pre-PETM levels over the next 70 kyr. The release of CH_4 into the atmosphere during the PETM could have played an important role in warming the climate[11,12], but because of its short residence time CH_4 can not explain the continued rise in temperatures following the termination of methane release. Atmospheric methane oxidizes to CO_2, which has a much longer residence time, but this CO_2 would have increased levels in the PETM atmosphere by only 70 to 160 p.p.m.v. (refs 1, 11), raising global temperature by less than 1 °C (ref. 12). These observations suggest that during the PETM the climate responded nonlinearly to changes in radiative forcing resulting from the addition of hydrate-derived carbon to the atmosphere.

Recently developed high-resolution stratigraphic records[3–6] and timescales[13] allow comparison of terrestrial and marine $\delta^{13}C$ records at the global scale. Important isotopic records are available for many sites, but we focus here on well-sampled records derived from characterized substrates that document the full shift in $\delta^{13}C$ values from a clearly defined, pre-PETM baseline through the CIE. These time series show that during a discrete, 60-kyr interval that includes peak PETM warming, the CIE in palaeosol carbonates from Wyoming (USA), Spain and China is consistently amplified by ~3‰ relative to that in marine records (Fig. 1d). Fossil soil organic matter (SOM) from terrestrial rocks in northern Wyoming[10] also documents an excursion ~1‰ larger than the marine CIE. This feature is common to the terrestrial $\delta^{13}C$ record on three continents, which strongly suggests that it is not a diagenetic artefact but reflects a discrete change in the partitioning of ^{13}C among the ocean, atmosphere, terrestrial biosphere and soils coinciding with PETM nonlinear climate system changes.

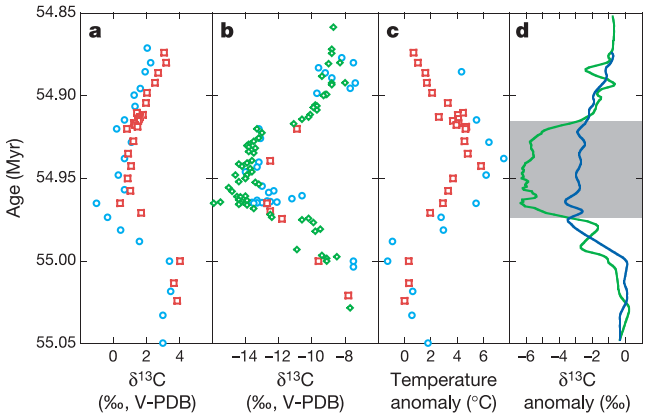

Figure 1 Marine and terrestrial records of the PETM, correlated to an age model for ODP site 690 (ref. 13, see Supplementary Information). **a**, Marine $\delta^{13}C$ records derived from the surface-dwelling genus *Acaranina* at ODP sites 690 (ref. 2, Southern Ocean, blue circles) and 1209 (ref. 3, subtropical Pacific Ocean, red squares). **b**, Palaeosol carbonate $\delta^{13}C$ records from northern Spain[6] (blue circles), Hunan, China[5] (red squares) and Wyoming, USA[4,30] (green diamonds). **c**, Temperature anomalies for sites 690 and 1209 calculated from monospecific $\delta^{18}O$ and Mg/Ca records, respectively (symbols as in **a**). **d**, Normalized composite carbon isotope curves for palaeosol carbonates (green) and planktonic foraminiferal carbonate (dark blue). Interval of terrestrial CIE amplification is shown in grey. $\delta^{13}C = \{[(^{13}C/^{12}C)_{sample}/(^{13}C/^{12}C)_{standard}] - 1\} \times 1{,}000$.

Here we integrate data and models to identify the carbon cycle processes responsible for amplifying the terrestrial CIE signal. Our analyses show that several processes could have made minor contributions to terrestrial CIE amplification. These include: (1) temperature effects on carbon isotope fractionation between CO_2 gas, dissolved inorganic carbon and $CaCO_3$ in the surface ocean and in soils; (2) changes in surface ocean carbonate ion concentration ($[CO_3^{2-}]$); and (3) changes in soil productivity and organic matter turnover rates.

Estimates of PETM warming from terrestrial[14] and surface ocean[2,3] records both fall between 5 and 10 °C, implying approximately equal temperature-driven decreases in palaeosol and foraminiferal carbonate $\delta^{13}C$ ($\delta^{13}C_{PC}$ and $\delta^{13}C_{FC}$ respectively) of 0.55–1.1‰ (ref. 15). Thus, the temperature effect exaggerates the magnitude of the CIE in these carbonate records relative to the shift in the other exogenic reservoirs, but does not contribute substantially to the offset between marine and terrestrial carbonate records.

Carbon release at the PETM would have affected ocean carbonate chemistry, causing a decrease in ocean pH and $[CO_3^{2-}]$ and an increase in $\delta^{13}C_{FC}$ (ref. 8). Mass balance calculations (see Supplementary Information) indicate that carbon addition to the ocean/atmosphere during the PETM could cause a 0.2–0.6‰ increase in $\delta^{13}C_{FC}$, thereby decreasing the CIE amplitude in marine records. If the mass of carbon released during the PETM has been severely underestimated[16,17], the $[CO_3^{2-}]$ effect may have been even larger. However, the $\delta^{13}C$ record of deep ocean foraminifera constrains the $[CO_3^{2-}]$ effect. Deepwater $[CO_3^{2-}]$ is less sensitive to carbon addition than surface water $[CO_3^{2-}]$ because of its greater overall carbon concentration and lower pH, and the $[CO_3^{2-}]$ effect should increase the $\delta^{13}C$ of surface ocean foraminifera more than that of deepwater forms. In fact, the CIE amplitude for surface-dwelling foraminifera during the PETM is larger than that for deep-dwellers. This observation has been attributed to changes in ocean circulation or productivity[2] but also suggests that $[CO_3^{2-}]$ change did not have an extreme effect on marine CIE records.

Soil processes determining the $\delta^{13}C$ offset between plants, SOM and soil CO_2 probably varied during the PETM. Experimental work has shown that warming and CO_2-fertilization can lead to increased rates of carbon input to soils (as root and leaf litter)[18] as well as increased turnover rates for SOM[19]. The $\delta^{13}C$ of soil carbonate is largely determined by that of soil CO_2 (ref. 20) and is sensitive to the rates of carbon input and SOM turnover, because they affect both the $\delta^{13}C$ of SOM ($\delta^{13}C_{SOM}$, from which most soil CO_2 is derived), and the mixing ratio of ^{13}C-enriched atmospheric and ^{13}C-depleted respired CO_2 within soil pores. We used a model of SOM and soil CO_2 dynamics[9] to examine the effects of changes in soil carbon processes on $\delta^{13}C_{PC}$ and $\delta^{13}C_{SOM}$ during the PETM (see Methods). Our simulations show that $\delta^{13}C_{PC}$ decreases in response to increased rates of carbon input to soils, and increases in response to increased turnover rates of SOM, largely as the result of changes in soil CO_2 concentration as more or less vegetation-derived CO_2 is concentrated in soil pores (Fig. 2a, b). In contrast, $\delta^{13}C_{SOM}$ is insensitive to the rate of carbon input to soil and increases in response to increased SOM turnover. These processes also cause substantial changes in the organic carbon content of soils (Fig. 2c), allowing us to constrain our simulations with measurements of the organic carbon concentrations of palaeosols from PETM and non-PETM strata (see Supplementary Information). Our results show no significant increase in carbon storage in PETM palaeosols, suggesting that increased organic inputs to PETM soils were balanced by increased SOM turnover rates. If 'reasonable' increases in ecosystem productivity during the PETM (that is, up to a doubling of SOM production rates) are combined with increased turnover so that soil carbon storage remains unchanged, our model

indicates that soil carbon dynamics can account for up to 0.9‰ of the terrestrial CIE amplification recorded by palaeosol carbonate (Fig. 2d), but at the same time cause $\delta^{13}C_{SOM}$ to increase by 0.6–1.0‰ (not shown).

In sum, the above effects account for half of the 3‰ CIE amplification in palaeosol carbonate, but leave a 1.7–2.1‰ difference between the modelled and observed SOM amplitudes.

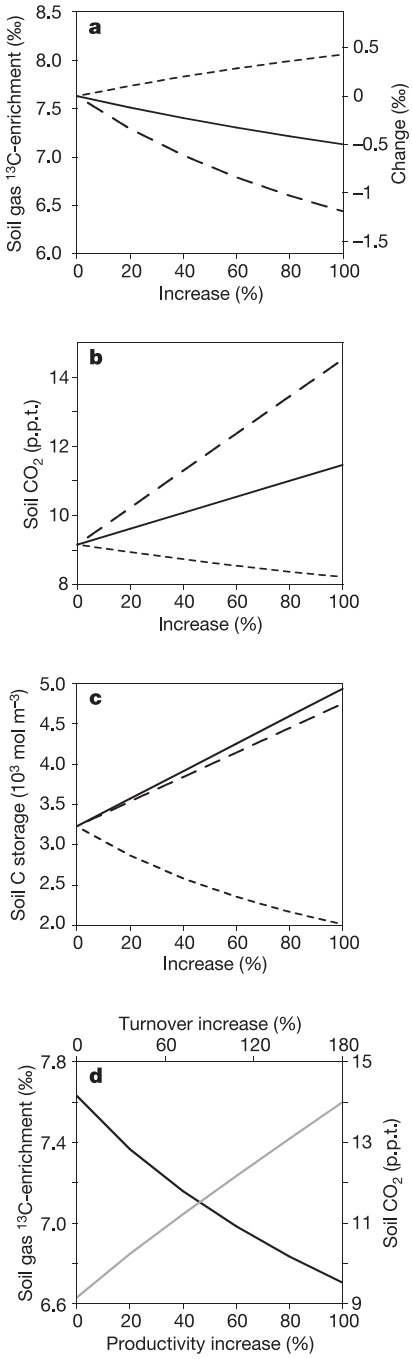

Figure 2 Results from soil carbon model runs. **a**–**c**, Effect of changing productivity above ground (solid black line) or below ground (long dashes) and of changing SOM decomposition rate (short dashes) on soil gas $\delta^{13}C$ (**a**), soil gas CO_2 concentration (**b**) and soil C storage (**c**). **d**, Effect of simultaneous changes in productivity and decomposition rate that result in no net increase in soil carbon storage. Soil gas ^{13}C-enrichment (black line) is the difference between soil $\delta^{13}CO_2$ at 1 m depth and vegetation $\delta^{13}C$. Soil CO_2 concentration (grey line) is given for 1 m depth, and organic carbon storage is integrated over the whole soil.

This implies that terrestrial plants increased their photosynthetic ^{13}C-discrimination by 1.5–2.1‰ during the PETM. We examined effects of changing water stress, the primary determinant of photosynthetic ^{13}C-discrimination, on the $\delta^{13}C$ values of PETM plants (see Methods). Temperature, relative humidity and soil water availability set the level of water stress. Higher PETM temperatures would have increased the transpiration demand on plants, decreasing ^{13}C-discrimination by 2–3‰ (Fig. 3). According to our simulations, it is only through substantial increases in relative humidity and soil moisture that plant ^{13}C-discrimination could have decreased despite climatic warming during PETM. We calculate that a minimum 20% increase in soil moisture and relative humidity would have been required during the PETM to account for the 1.5–2.1‰ increase in plant ^{13}C-discrimination (Fig. 3). About 85% of this change in vegetation $\delta^{13}C$ would be transferred to soil CO_2 and carbonate; a loss of 15% of the signal occurs owing to dilution by atmosphere-derived CO_2 within soils.

Taken together, our analysis of marine and terrestrial carbon cycle processes provides a coherent explanation for PETM CIE amplification in terrestrial SOM and palaeosol carbonate (Table 1). Notably, the solution requires a 20–25% increase in soil and atmospheric moisture throughout the northern mid-latitudes and a near doubling in the rate of carbon cycling through terrestrial ecosystems. These changes are consistent with clay mineral records that suggest enhanced continental weathering across these regions during the PETM[21]. Given the protracted duration and stable magnitude of the terrestrial CIE amplification, these changes do not fit a model of linear response to methane release, but rather seem to represent a discrete, transient switch in climate state. The cause and effect relationships between methane hydrate destabilization and the PETM climate state switch, as well as the climate system changes underlying the PETM wet climate state, are currently unknown. Although atmospheric moisture is a powerful greenhouse gas and may have contributed to PETM warming, it is an internal component of the climate system. Persistent, elevated relative humidity during the PETM must represent a feedback responding to some other change in the climate system. This change remains to be identified, but potential candidates include a change in ocean circulation and heat transport[12], higher levels of atmospheric CO_2 due to changes in ocean circulation and chemistry[2], or higher CH_4 concentrations sustained by elevated fluxes from wetlands.

Recognition of a discrete climate state shift during the PETM has important implications for understanding the evolution of greenhouse climate at the Palaeocene/Eocene boundary and the potential evolution of future climate. Climate system changes associated with the PETM wet climate state help resolve the discrepancy between the observed temperature changes and forcing mechanisms suggested thus far. Both the buildup of tropospheric water vapour and lack of carbon sequestration by soils would have amplified and helped to sustain PETM warmth. In contrast, increases in plant productivity, soil CO_2 and soil moisture associated with the PETM wet climate state would have increased silicate weathering and the delivery of nutrients and alkalinity to the oceans, increasing the burial of

Table 1 **Proposed model for PETM terrestrial CIE amplification**

	$\Delta(\Delta^{13}C_{(V-FC)})^*$	$\Delta(\Delta^{13}C_{(SOM-FC)})^*$	$\Delta(\Delta^{13}C_{(PC-FC)})^*$
5 °C warming†	−0.55‰	−0.55‰	0‰
$[CO_3^{2-}]$ effect	0.5‰	0.5‰	0.5‰
Balanced 1.8 × soil productivity‡	0‰	−1.0 to −0.6‰	0.8‰
+20% RH and soil moisture	2.0‰	2.0‰	1.7‰
Total	1.95‰	0.95 to 1.35‰	3.0‰
Observed	n.a.	~1.0‰	~3.0‰

RH, relative humidity; n.a., not available
*Change in $\delta^{13}C$ offset between terrestrial vegetation (V), soil organic matter (SOM) or palaeosol carbonate (PC) and surface ocean foraminiferal carbonate (FC).
†Equal warming assumed at marine and terrestrial sites.
‡Increased litter input to soils balanced by increased SOM turnover rate.

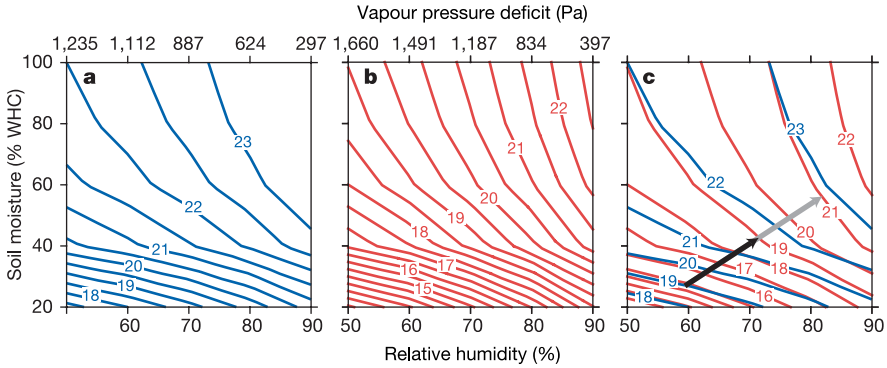

Figure 3 Photosynthetic ^{13}C-discrimination by tropical evergreen C_3 plants. Isotopic discrimination (labelled colour contours, in ‰) is given for temperatures of 20 °C (pre-PETM, **a**) and 25 °C (PETM, **b**) and a range of atmospheric and soil moisture conditions. **c**, Discrimination shown for both temperatures superimposed on common axes for relative humidity and soil moisture (colours as in **a**, **b**). At both mean annual temperatures, photosynthetic ^{13}C-discrimination increases (plant δ^{13}C decreases) in response to increased relative humidity or soil moisture (as a percentage of soil water holding capacity, WHC). Arrows in **c** show increases in relative humidity (black) and soil moisture (grey) required to hold plant δ^{13}C constant at the estimated pre-PETM value (19‰, see Supplementary Information) and to account for the observed 1.5–2.1‰ decrease in plant δ^{13}C during the PETM.

carbon in marine carbonate rocks[13]. This negative feedback probably contributed to climate recovery following the PETM, but temperature stabilization and recovery lagged the climate state switch by ~30–40 kyr. Given the current exponential increase in atmospheric CO_2 and other greenhouse gases, determining the complete sequence of events associated with the PETM climate state change and assessing the generality of the state change through study of similar episodes of greenhouse warming in the Earth's history[22,23] seems critical. □

Methods

Soil carbon model

The steady-state model for soil organic carbon and CO_2 was described in ref. 9. It includes input functions for organic carbon above and below ground and for root-respired CO_2, along with vertical transport, microbially mediated transformation of organic carbon among three discrete organic carbon pools, heterotrophic respiration, and biological and physical ^{13}C-fractionating processes associated with microbial respiration and diffusion of CO_2. For initial conditions, we used model parameter values fitted to data from a carbonate-bearing chernozem[9] and plant ^{13}C-discrimination (Δ) = 19‰. In the initial conditions, the model soil stores 3,229 mol C m^{-2} and at 1 m depth has a CO_2 concentration of 9.16 parts per thousand (p.p.t.) with soil gas δ^{13}C enriched by 7.6‰ relative to vegetation, bulk SOM enriched by 2.4‰ relative to vegetation, and stable[9] SOM enriched by 2.9‰ relative to vegetation. We tested the sensitivity of soil CO_2 concentration and δ^{13}C values, and also SOM storage and δ^{13}C values, to changes in model parameters by incrementally changing them from their initial values, either individually or together, and re-integrating the model. The tests reported here were performed using ranges of Δ values (19–23‰), plant productivity rates above ground (30 to 60 mol C m^{-2} yr^{-1}) and below ground (20 to 40 mol C m^{-2} yr^{-1}), and soil carbon turnover rate (0.2 to 0.4, 0.01 to 0.02, and 0.001 to 0.002 yr^{-1} for carbon cycling at 'fast', 'slow' and 'stable' rates, respectively). These tests assume that root respiration varies proportionately with productivity below ground. We also tested the effects of decreased microbial assimilation efficiency[9] (0.4 to 0.2 mol C assimilated per mol C consumed for fast and slow cycling carbon, and 0.2 to 0.1 for stable carbon levels); the results were very similar to those obtained with increased turnover rate and are not shown here. All other model parameters were held constant, and simulations were run at an atmospheric CO_2 concentration of 1,500 p.p.m. Results reported here are for depth-integrated SOM storage and for soil gas and bulk and stable SOM at 1 m below the soil surface.

Modelling plant carbon isotope fractionation

Discrimination against ^{13}C (Δ) by leaves was calculated using the well-validated model[7] linking Δ to leaf gas exchange, which is given as: $\Delta = a + (b - a) \times c_i/c_a$, where a is fractionation associated with diffusion (4.4‰), b is fractionation associated with the enzyme Rubisco (27‰), and c_i and c_a are the intercellular and atmospheric CO_2 partial pressures respectively. Experimental and geological evidence indicates that terrestrial plant δ^{13}C values are insensitive to changes in CO_2 (ref. 24), but that water stress is the primary factor determining the magnitude of terrestrial plant photosynthetic ^{13}C-discrimination[7]. We calculated equilibrium c_i/c_a ratios at c_a = 1,500 p.p.m.v. over a range of humidity, temperature and soil moisture content values using a mechanistic model of photosynthetic carbon uptake[25] coupled to a model of stomatal behaviour[26]. The coupled model incorporated the effects of leaf-to-air difference in the molar concentration of water vapour on stomatal conductance and accounted for soil moisture based on the reductions in stomatal conductance that occur with soil drying[27]. All simulations used maximum rates of carboxylation activity (94.1 μmol m^{-2} s^{-1}) and photosynthetic electron transport (183.1 μmol m^{-2} s^{-1}), characteristic of the deciduous and evergreen tropical forests[28] that predominated at the continental PETM sites investigated[29].

Received 25 March; accepted 12 October 2004; doi:10.1038/nature03115.

1. Dickens, G. R., Castillo, M. M. & Walker, J. C. G. A blast of gas in the latest Paleocene; simulating first-order effects of massive dissociation of oceanic methane hydrate. *Geology* **25,** 259–262 (1997).
2. Kennett, J. P. & Stott, L. D. Abrupt deep-sea warming, palaeoceanographic changes and benthic extinctions at the end of the Palaeocene. *Nature* **353,** 225–229 (1991).
3. Zachos, J. C. *et al.* A transient rise in tropical sea surface temperature during the Paleocene-Eocene thermal maximum. *Science* **302,** 1551–1554 (2003).
4. Bowen, G. J. *et al.* in *Paleocene-Eocene Stratigraphy and Biotic Change in the Bighorn and Clarks Fork Basins, Wyoming* (ed. Gingerich, P. D.) 73–88 (Univ. of Michigan Museum of Paleontology, Ann Arbor, Michigan, 2001).
5. Bowen, G. J. *et al.* Mammalian dispersal at the Paleocene/Eocene boundary. *Science* **295,** 2062–2065 (2002).
6. Schmitz, B. & Pujalte, V. Sea-level, humidity, and land-erosion records across the initial Eocene thermal maximum from a continental-marine transect in northern Spain. *Geology* **31,** 689–692 (2003).
7. Farquhar, G. D., Ehleringer, J. R. & Hubrick, K. T. Carbon isotope discrimination and photosynthesis. *Annu. Rev. Plant Physiol. Plant Mol. Biol.* **40,** 503–537 (1989).
8. Spero, H. J., Bijma, J., Lea, D. W. & Bemis, B. E. Effect of seawater carbonate concentration on foraminiferal carbon and oxygen isotopes. *Nature* **390,** 497–500 (1997).
9. Bowen, G. J. & Beerling, D. J. An integrated model for soil organic carbon and CO_2: implications for paleosol carbonate pCO_2 paleobarometry. *Glob. Biogeochem. Cycles* **18,** doi:10.1029/2003GB002117 (2004).
10. Magioncalda, R., Dupuis, C., Smith, T., Steurbaut, E. & Gingerich, P. D. Paleocene-Eocene carbon isotope excursion in organic carbon and pedogenic carbonate: Direct comparision in a continental stratigraphic section. *Geology* **32,** 553–556 (2004).
11. Schmidt, G. A. & Shindell, D. T. Atmospheric composition, radiative forcing, and climate change as a consequence of a massive methane release from gas hydrates. *Paleoceanography* **18,** doi:10.1029/2002PA000757 (2003).
12. Renssen, H., Beets, C. J., Fichefet, T., Goosse, H. & Kroon, D. Modeling the climate response to a massive methane release from gas hydrates. *Paleoceanography* **19,** doi:10.1029/2003PA000968 (2004).
13. Farley, K. A. & Eltgroth, S. F. An alternative age model for the Paleocene-Eocene thermal maximum using extraterrestrial He-3. *Earth Planet. Sci. Lett.* **208,** 135–148 (2003).
14. Fricke, H. C. & Wing, S. L. Oxygen isotope and paleobotanical estimates of temperature and δ^{18}O - latitude gradients over North America during the Early Eocene. *Am. J. Sci.* **304,** 612–635 (2004).
15. Friedman, I. & O'Neil, J. R. in *Compilation of Stable Isotope Fractionation Factors of Geochemical Interest* (ed. Fleischer, M.) 1–12 (US Geological Survey, Reston, Virginia, 1977).
16. Kurtz, A. C., Kump, L. R., Arthur, M. A., Zachos, J. C. & Paytan, A. Early Cenozoic decoupling of the global carbon and sulfur cycles. *Paleoceanography* **18,** doi:10.1029/2003PA000908 (2003).
17. Svensen, H. *et al.* Release of methane from a volcanic basin as a mechanism for initial Eocene global warming. *Nature* **429,** 542–545 (2004).
18. Schäfer, K. V. R. *et al.* Exposure to an enriched CO_2 atmosphere alters carbon assimilation and allocation in a pine forest ecosystem. *Glob. Change Biol.* **9,** 1378–1400 (2003).
19. Macdonald, N. W., Zak, D. R. & Pregitzer, K. S. Temperature effects on kinetics of microbial respiration and net nitrogen and sulfur mineralization. *Soil Sci. Soc. Am. J.* **59,** 233–240 (1995).
20. Cerling, T. E. The stable isotopic composition of modern soil carbonate and its relationship to climate. *Earth Planet. Sci. Lett.* **71,** 229–240 (1984).
21. Bolle, M. P. & Adatte, T. Palaeocene-early Eocene climatic evolution in the Tethyan realm; clay mineral evidence. *Clay Miner.* **36,** 249–261 (2001).
22. Gröcke, D. R., Hesselbo, S. P. & Jenkyns, H. C. Carbon-isotope composition of Lower Cretaceous fossil wood: ocean-atmosphere chemistry and relation to sea-level change. *Geology* **27,** 155–158 (1999).
23. Hesselbo, S. P. *et al.* Massive dissociation of gas hydrate during a Jurassic oceanic anoxic event. *Nature* **406,** 392–395 (2000).
24. Tu, T. T. N., Kürschner, W. M., Schouten, S. & Van Bergen, P. F. Leaf carbon isotope composition of

fossil and extant oaks grown under differing atmospheric CO_2 levels. *Palaeogeogr. Palaeoclimatol. Palaeoecol.* **212,** 199–213 (2004).
25. Farquhar, G. D., von Caemmerer, S. & Berry, J. A. A biochemical model of photosynthetic CO_2 assimilation in leaves of C3 species. *Planta* **149,** 78–90 (1980).
26. Leuning, R. A critical appraisal of a combined stomatal-photosynthesis model for C3 plants. *Plant Cell Environ.* **18,** 339–355 (1995).
27. Granier, A., Biron, P., Bréda, N., Pontallier, J. Y. & Saugier, B. Transpiration of trees and forest stands: short-term and long-term monitoring using sapflow methods. *Glob. Change Biol.* **2,** 265–274 (1996).
28. Beerling, D. J. & Quick, W. P. A new technique for estimating rates of carboxylation and electron transport in leaves of C-3 plants for use in dynamic global vegetation models. *Glob. Change Biol.* **1,** 289–294 (1995).
29. Sewall, J. O., Sloan, L. C., Huber, M. & Wing, S. Climate sensitivity to changes in land surface characteristics. *Glob. Planet. Change* **26,** 445–465 (2000).
30. Koch, P. L., Zachos, J. C. & Dettman, D. L. Stable isotope stratigraphy and paleoclimatology of the Paleogene Bighorn Basin (Wyoming, USA). *Palaeogeogr. Palaeoclimatol. Palaeoecol.* **115,** 61–89 (1995).

Supplementary Information accompanies the paper on **www.nature.com/nature**.

Acknowledgements We thank W. Cheng, G. Dickens, D. Schrag, L. Sloan and F. I. Woodward for comments. Funding was provided by a National Science Foundation Biocomplexity grant. G.J.B. was supported by the National Science Foundation Graduate Research Fellowship Program, and D.J.B. gratefully acknowledges funding from the Royal Society and the Leverhulme Trust.

Competing interests statement The authors declare that they have no competing financial interests.

Correspondence and requests for materials should be addressed to G.J.B. (gbowen@biology.utah.edu).

Indirect reciprocity can stabilize cooperation without the second-order free rider problem

Karthik Panchanathan & Robert Boyd

Center for Behavior, Evolution, and Culture and Department of Anthropology, University of California, Los Angeles, California 90095, USA

Models of large-scale human cooperation take two forms. 'Indirect reciprocity'[1] occurs when individuals help others in order to uphold a reputation and so be included in future cooperation. In 'collective action'[2], individuals engage in costly behaviour that benefits the group as a whole. Although the evolution of indirect reciprocity is theoretically plausible[3–6], there is no consensus about how collective action evolves. Evidence suggests that punishing free riders can maintain cooperation[7–9], but why individuals should engage in costly punishment is unclear. Solutions to this 'second-order free rider problem' include meta-punishment[10], mutation[11], conformism[12], signalling[13–15] and group-selection[16–18]. The threat of exclusion from indirect reciprocity can sustain collective action in the laboratory[19]. Here, we show that such exclusion is evolutionarily stable, providing an incentive to engage in costly cooperation, while avoiding the second-order free rider problem because punishers can withhold help from free riders without damaging their reputations. However, we also show that such a strategy cannot invade a population in which indirect reciprocity is not linked to collective action, thus leaving unexplained how collective action arises.

To show that indirect reciprocity can stabilize collective action without the second-order free rider problem, we consider a large population subdivided into randomly formed social groups of size n. Social life consists of two stages. First, individuals decide whether or not to contribute to a one-shot collective action game at a net personal cost C in order to create a benefit B shared equally amongst the $n - 1$ other group members, where $B > C$. Second, individuals engage in a multi-period 'mutual aid game'[4], a form of indirect reciprocity that is well suited to a population structured into groups. The dynamics of the mutual aid game are very similar to other models of indirect reciprocity[3,6] so our results should generalize to other social exchange systems. In each period of the mutual aid game, one randomly selected individual from each group is 'needy'. Each of his $n - 1$ neighbours can help him an amount b at a personal cost c, where $b > c > 0$. Each individual's behavioural history is known to all group members. This assumption is essential because it is known that indirect reciprocity cannot evolve when information quality is poor[6]. The mutual aid game repeats with probability w and terminates with probability $1 - w$, thus lasting for $1/(1 - w)$ periods on average. Afterwards, individuals reproduce on the basis of payoffs accumulated over both stages, relative to the whole population, and then die.

Individuals are characterized by one of three heritable strategies: 'Defector', 'Cooperator', and 'Shunner'. Defectors do not contribute to the collective action, nor do they help during the mutual aid game. Cooperators contribute to the collective action and try to help all needy recipients during mutual aid. With probability e, however, Cooperators mistakenly fail to help recipients of good reputation in the mutual aid game owing to an implementation error[6] (See Box 1 for details). Shunners contribute to the collective action and then try to help those needy individuals who have good reputations during the mutual aid game, but mistakenly fail owing to errors with probability e just like Cooperators. Shunners never help needy recipients who are in bad standing.

All individuals begin their lives in good standing. Failure to contribute to the collective action results in a lifetime of bad standing. If an individual has contributed during the collective action stage, she temporarily loses her good standing if she fails to help a recipient of good reputation during the mutual aid game, either through intention or error. She can, however, restore her good standing by helping a needy recipient in some future period. Our results do not depend on the assumption that the reputations

Box 1
Errors in models of reciprocity and punishment

As in previous models of indirect reciprocity[3,5,6], errors play a crucial role in our analysis. These errors should not be thought of as part of an inherited strategy. Instead, they represent exogenous factors like sickness or accidents that prevent actors from helping despite an intention to do so. In our model, all group members, including the actor, know when an error has occurred. These 'implementation' errors are contrasted with 'perception' errors, in which individuals differ in their beliefs about who cooperated and who defected[6]. We have not analysed the effect of perception errors because these errors add sufficient mathematical complexity that analysis becomes intractable. As a result, it is unclear how perception errors affect the evolution of indirect reciprocity[3,6]. In addition, we do not consider errors in which individuals mistakenly help a recipient of bad reputation during the mutual aid game, nor errors during the collective action game, because both such errors complicate the model without qualitatively altering the results.

Previous models of collective action and costly punishment[10–12,18] have shown that implementation errors of the type we consider here undermine the evolution of collective action. To see why, suppose that there are no defecting strategies and that behaviour is error-free. In this case, selection cannot distinguish between strategies that cooperate and punish defectors and strategies that cooperate but do not punish. There is never a need to punish, so there is no second-order free rider problem. If actors occasionally defect by mistake, however, strategies that punish must do so at a personal cost. Selection will now favour strategies that cooperate but do not punish (second-order free riders). As a result, strategies that punish free riders decline and eventually defectors can invade and take over.